UNIVERSITY OF CALIFORNIA SAN DIEGO

Variations in P_n seismic velocities and lithospheric thermal structure across Mendocino fracture zone, eastern Pacific ocean

A thesis submitted in partial satisfaction of the
requirements for the degree Master of Science

in

Earth Sciences

by

Guilherme Weber Sampaio de Melo

Committee in charge:

Professor David Sandwell, Chair
Professor Steven Constable
Professor Peter Shearer

2022

The Thesis of Guilherme Weber Sampaio de Melo is approved, and it is acceptable in quality and form for publication on microfilm and electronically.

University of California San Diego

2022

DEDICATION

To my Family, Solina Sampaio, Jose Sampaio

EPIGRAPH

Never give up on what you really want to do.

The person with big dreams is more powerful than one with all the facts.

Albert Einstein

TABLE OF CONTENTS

LIST OF FIGURES

LIST OF TABLES

ACKNOWLEDGEMENTS

I am fully grateful to Professor David Sandwell for his research interest, for giving me support, and for receipt me as a master's student at Scripps. Your opportunity allowed me to continue and encourage me to advance my life as a researcher after a bad moment.

I would also like to acknowledge Professor Steven Constable for providing me access to the project data to work on this thesis, giving me support for my work at Scripps, as also for being part of my thesis committee.

Thank you to Professor Peter Shearer be part of the committee and for every guidance and opinion provided to me during the analysis and results from observations of the seismologic activity and measurement of the Pn velocities. Thank you also Professor Ross Parnell-Turner for the feedback on the thesis draft.

Thanks for all the lively, fun, and cheerful moments with you folks on our graduate first-year students 2021 team, mainly Anupam Patel, Nicolas DeSalvio, John Rekoske, Jeremy Wong, Xiaoyu Zou, and Jenna Yun. I will miss you!

This work was supported by the National Science Foundation through OCE-1736590, and UC Shipfunds for the shipping time. Thanks to Valeria Reyes for the data collection. This thesis, in full, is in preparation for publication as it may appear in a journal. de Melo, Guilherme W. S.; Sandwell, David T.; Constable, Steven. The thesis author was the primary investigator and author.

VITA

2016	Lic. in Physics, Federal University of Rio Grande do Norte, Brazil
2021	B.S. in Geophysics, Federal University of Rio Grande do Norte, Brazil
2019	M.S. in Geophysics, Federal University of Rio Grande do Norte, Brazil
2022	M.S. in Earth Sciences, University of California San Diego, United States

ABSTRACT OF THE THESIS

Variations in P_n seismic velocities and lithospheric thermal structure across Mendocino fracture zone, eastern Pacific ocean

by

Guilherme Weber Sampaio de Melo

Master of Science in Earth Sciences

University of California San Diego, 2022

Professor David Sandwell, Chair

Oceanic lithosphere varies considerably around the globe, with different geodynamic settings that contribute to various models of seismotectonic activity over the tectonic plate boundaries. Lithospheric age, temperature, and thickness are three fundamental features to understanding geodynamic behavior. However, the model in which they influence seismic wave propagation is poorly understood over different oceanic areas. Here, we analyze the behavior of seismic velocities and lithospheric thickness from measurements of uppermost mantle-Moho P_n velocities and thermal structure modeling over the Mendocino fracture zone (MFZ), eastern Pacific ocean. We use pressure data obtained from 21 ocean-bottom electromagnetic instruments

deployed across the MFZ in October-December of 2017. We present results obtained from 19 regional earthquakes of global catalogs with magnitudes $\geq$2.5, with their epicenters raging from 311 to 588 km away. We obtained 205 Pn ray paths with P_n velocities ranging from 8.01$\pm$0.1 to 8.48$\pm$0.2 km/s. The results show correlations between the increase in P_n velocities with the lithospheric age as well as a decrease in velocity with increasing temperature. Also, the highest velocities are directed near parallel to the fracture zone and perpendicular to the ridge axis. Therefore, our results demonstrate the MFZ particular area is fundamental to the understanding of seismic wave propagation over the uppermost mantle-Moho zone and the lithosphere thickness dependence over geodynamic features.

Chapter 1

Introduction

Oceanic fracture zones (FZ) are the inactive extensions of the oceanic transform faults (*Menard and Atwater*, 1969), which represent a discontinuity in the age and temperature of the lithosphere. Cooling of the oceanic lithosphere causes an increase in thickness with age resulting in a change in thickness across the FZ (*Mutter and Karson*, 1992). Compressional seismic waves that reflect off the Moho layer (P_n phase) in oceans and propagate through the uppermost mantle are key to understanding the effect of the heterogeneity in the oceanic lithosphere. Seismic profiles have been used to show the seismic velocity structure of the uppermost mantle. However, there are some variations in P_n velocity in different ocean basins, perhaps due to different spreading rates. *Growe et al.* (2021) used seismic refraction and wide-angle in the St. Paul fracture zone, equatorial Atlantic ocean, with 40-50 Ma oceanic lithosphere in the south and 70 Ma in the north sides to show P_n velocities variation between 7.9-8.0 km/s range. Similarly, seismic experiments obtained in Chain fracture zone, with 10-24 Ma lithosphere age changing from north to south side, presented P_n velocities of 7.8 to 8.0 km/s, respectively (*Marjanović et al.*, 2020). Furthermore, using hydrophone records, measurements have shown an average P_n velocity estimation varying from 7.8 to 8.5 km/s between the eastern Pacific (*Dziak et al.*, 2004) and equatorial Atlantic (*de Melo et al.*, 2021). In addition, tomography analysis using P_n phases has presented uppermost mantle P_n velocities ranging from 7.4-8.3 km/s using ocean-bottom seismometers deployed in Juan de Fuca and Gorda plates (*VanderBeek and Toomey*, 2019).

Measurements using hydrophone P_n records provided estimations with an average of 8.0 km/s and 7.9 km/s on the Juan de Fuca and Pacific plates (*Slack et al.*, 1999). Also, *Henstock and Levander* (2003) showed P_n velocities of approximately 7.5-8.0 km/s using seismic profiles along the Mendocino triple junction. Despite these studies, the dependence of lithospheric age or temperature over the uppermost mantle velocities is poorly constrained in ocean basins, which is crucially important to understanding how much the spreading rates, ages, or thermal structure influence the mechanical process of seismic wave propagation along the lithosphere.

Here, we present measurements of P_n wave velocities derived from travel times between 19 regional earthquakes and 13 seafloor instruments deployed across Mendocino fracture zone (MFZ) in 2017 (*Reyes-Ortega et al.*, 2019). We investigate the P_n velocity versus lithospheric age and seismic anisotropy. Finally, we observe correlations between the temperature of the uppermost mantle-Moho layer and lithospheric age, which demonstrate a direct dependence on the crustal thickness and lithospheric age.

1.1 Mendocino Fracture Zone

Mendocino fracture zone (MFZ) is located offshore of northern California on Pacific Plate. Our study region has a north-to-south age offset of 25 Ma. The large topographic scarps of MFZ formed as a response to the isostatic balance in the lithosphere during the subduction of the ancient Farallon plate over the current Cascadia subduction zone in North American plate from the middle to late Tertiary (*Glazner and Schubert* 1985; *Lonsdale* 2005). Two small tectonic plates compose the south area of Cascadia in the present day: Gorda at the southern, and Juan de Fuca in the central zone (Fig.1.1). Mendocino composes the southern border of Cascadia formed by a triple junction between Gorda, the San Andreas fault, and the Pacific plates. The ridges composing the western boundary of the Gorda plate are spreading at intermediate rates ranging from 48.1 to 51.5 mm/year (*DeMets et al.*, 2010). Mendocino transform ($\sim$240 km long) is seismically active with shallow right-lateral strike-slip earthquakes as large as Mw 7.1 (*Dengler et al.*, 1995), and Mw 7.2 in oblique strike-slip faults inside the Gorda plate (*Rollins and Stein*, 2010). Also, in Juan de Fuca plate, the Blanco transform ($\sim$350 km long) is a seismotectonic active with strike-slip earthquakes until Mw 6.6 (*Braunmiller and Nábělek*, 2008).

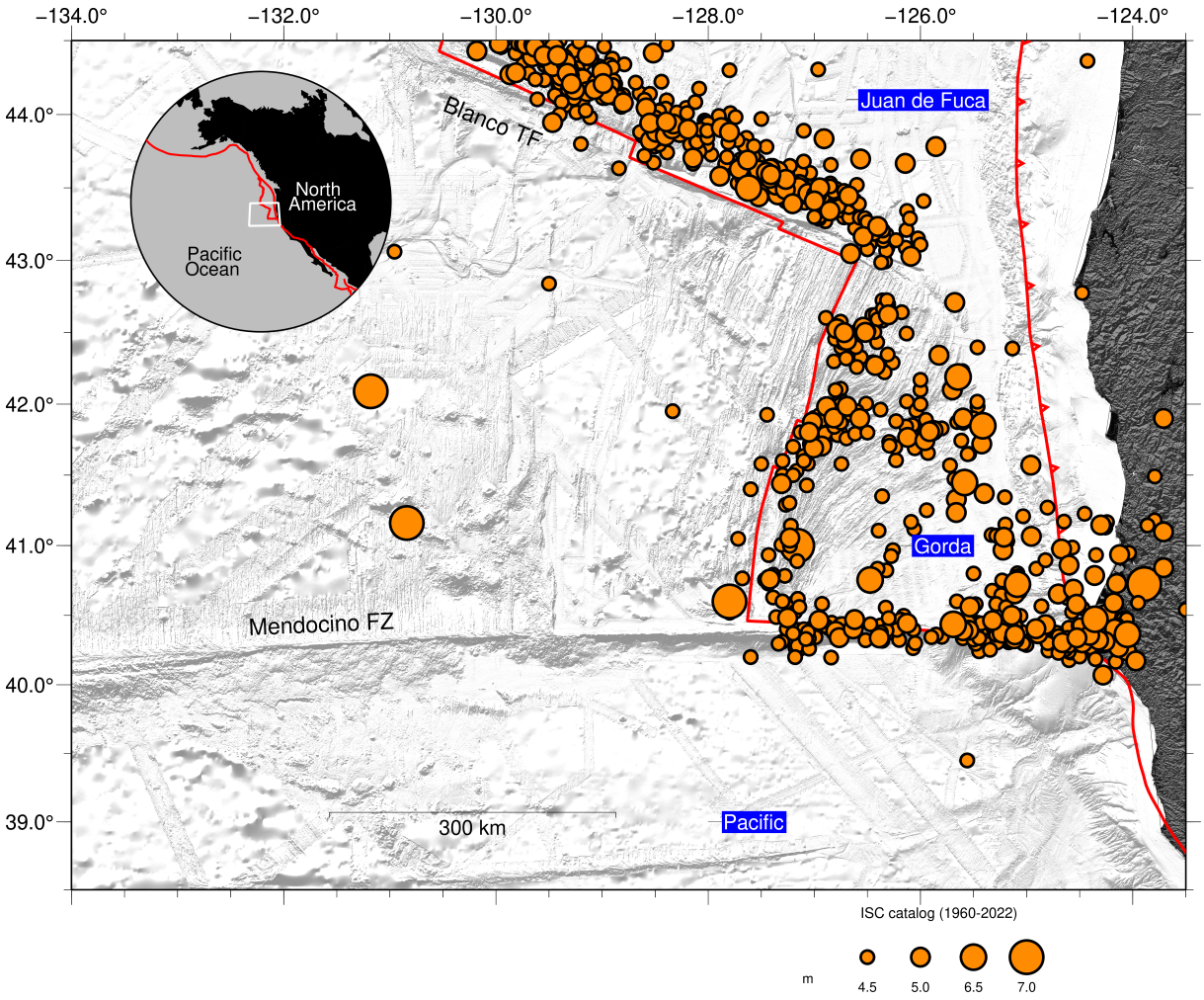

Figure 1.1. Shaded map over the study area in eastern Pacific ocean. Orange circles are the complete seismicity cataloged by International Seismology Center (ISC) between 1960 and 2022.

Chapter 2

Pn velocity and lithospheric temperature

2.1 Data and seismicity

This study utilizes data collected by a set of 21 ocean-bottom electromagnetic (OBEM) instruments deployed in a 200 km long N-S array across the Mendocino Fracture Zone (MFZ) between October and December of 2017 (*Reyes-Ortega et al.*, 2019). The data was acquired by a differential pressure gauge (*Cox et al.*, 1984) hydroacoustic channel sampling in 62.5 Hz. Nineteen of the 21 instruments produced data analyzed in our study. The location of the instruments across the MFZ is shown in the bathymetric map of the study area (Fig.2.1).

During the 61-67 days deployment, 29 regional earthquakes were large enough to provide travel time data in global networks (WILBER3/IRIS, Incorporated Research Institutions of Seismology; ISC, International Seismology Center) in 38.5 to 44.5° latitude and -134 to -123.75° longitude. Their epicenters occur located over the boundaries of the Gorda and Juan de Fuca plates with the Pacific. All earthquakes have been located with epicentral distances ranging from 311 to 588 km from the OBEM instruments, and with magnitudes ranging from Ml 2.0 to 5.3 Mw. We analyzed data of the complete record period using the Seismic Analysis Code package (*Goldstein et al.*, 2003). The origin times reported by the WILBER3 and ISC catalogs were used to calculate approximate arrival times of all earthquake catalogs in records using the IASP91 global travel-time model (*Kennett and Engdahl*, 1991). A highpass filter of 2.5 Hz was applied to remove unwanted noise, without any waveform observed in a frequency range lower

than that. After filtering, we analyzed the arrival times of 19 events with a magnitude above 2.5 Ml (Table.1), picking manually the P_n phases in the records. A total of 205 ray paths were identified in the analysis (Fig.2.2). The other 10 events not included in (Table.1) have epicenters located more distant, deepest, and over the continental drift (Fig.2.3). These features of the 10 not-analyzed events are difficult the observation by the rapid attenuation and loss of amplitude of the P_n phase in the western area continental (*Buehler and Shearer*, 2014).

Next, we manually picked the P_n phase arrival times at the beginning of the earthquake waveform, using a reference to the arrival time of the IASP91 model as a guide. We estimate an uncertainty of 1s in P_n piking for all earthquakes. The 19 events were recorded only by 13 of the 19 working instruments. Signal with high noise or issues was identified in the signal of the other six instruments. The other 10 earthquakes were located in the longest distance and weaker magnitudes without a good signal enough to picking of the P_n phase (signal-to-noise ratio $<$1.7). Every earthquake analyzed was recorded with a high signal-to-noise ratio ($>$3.0) by at least seven instruments, and all instruments recorded at least 13 events.

Table 2.1. Complete list of the 19 earthquakes with P_n analyzed in this study (mb: body wave magnitude; ML: local magnitude; Mw: moment magnitude).

Date	Time	Lat, °	Long, °	Depth, km	Mag	Mag.Scale	Catalog
2017-10-10	06:10:01	44.0507	-128.7884	10.0	3.9	mb	ISC
2017-10-10	06:38:37	44.0308	-128.6702	13.0	3.9	mb	ISC
2017-10-10	07:26:21	43.6701	-129.3952	14.8	3.4	ML	NEIC
2017-10-13	16:55:19	43.4803	-127.1229	14.0	5.4	Mw	ISC
2017-10-15	19:37:07	41.8142	-126.7256	10.0	2.8	ML	NEIC
2017-10-17	14:02:30	41.2886	-126.8083	7.2	2.5	ML	NEIC
2017-10-17	14:58:45	41.2066	-127.4400	8.7	3.0	ML	NEIC
2017-10-17	15:12:40	41.2260	-127.0948	9.6	2.7	ML	NEIC
2017-10-17	15:20:19	41.2808	-126.9770	10.5	2.9	ML	NEIC
2017-10-17	15:22:13	41.2770	-127.1684	8.5	2.8	ML	NEIC
2017-10-17	16:54:44	41.1741	-127.5145	8.4	2.8	ML	NEIC
2017-10-17	22:59:08	40.4304	-126.9485	10.0	3.2	ML	NEIC
2017-10-18	01:30:10	41.1997	-127.1635	10.0	4.2	mb	NEIC
2017-10-27	06:39:51	43.9346	-127.9434	10.0	3.1	ML	NEIC
2017-10-28	10:41:45	43.4022	-127.3797	10.0	3.0	ML	NEIC
2017-11-09	15:58:57	40.3940	-125.0730	27.5	2.9	Md	NEIC
2017-11-15	04:54:47	40.2980	-124.5277	21.7	3.0	ML	ISC
2017-11-17	15:12:56	42.0933	-125.9714	10.0	3.2	ML	NEIC
2017-11-24	17:36:12	43.0858	-126.3128	10.0	4.7	Mw	NEIC

2.2 One-Directional velocity estimations

Both compressional waves (P) and shear waves (S) propagate in the upper mantle. P waves have at least two main phases over the layers close to the surface: P_g that propagates into the crust directly of the source to the seismic station, and P_n wave which is a P wave bottoming in the uppermost mantle (Fig.2.4). We used in analysis the P_n waves generated by earthquakes of oceanic transform fault or mid-ocean ridges trend to intercept layers deeper through the uppermost mantle due to the thin crust existent with a brittle-ductile limitation commonly situated already beneath the crust (Fig.2.4, lower, *Storchak et al.* (2003)).

P_n waves propagate with an average velocity range of 8.0-8.2 km/s in the oceanic lithosphere (*Searle*, 2013). However, P_n ray paths can travel through different layers in the uppermost mantle, due to the large heterogeneity in layers beneath the Moho during the source-receiver travel (*Buehler and Shearer*, 2010). To obtain estimations of P_n velocities (u_{P_n}) traveling in the uppermost mantle, we applied the following equation:

$$u_{P_n} = \frac{\Delta_{se} - \Delta_{P_n}}{(\tau_s - \tau_e) - \tau_{P_n}} \tag{2.1}$$

It is a direct calculation using the epicentral distance Δ_{se} (km), with origin time of event (τ_e) and arrival time in station (τ_s) in s, similarly to methodology used by *Slack et al.* (1999), *Dziak et al.* (2004), and *de Melo et al.* (2021). However, we are using instruments deployed directly on the seafloor, such that the correction to P_n ray path will be applied to the distance (Δ_{P_n}) and time (τ_{P_n}) between the surface source to the surface point over the turning point of P_n wave (*Shearer*, 2019), given by

$$\Delta_{P_n} = p\frac{z}{(u^2 - p^2)^{\frac{1}{2}}} \tag{2.2}$$

$$\tau_{P_n} = \frac{u^2}{(u^2 - p^2)^{\frac{1}{2}}} z \tag{2.3}$$

where $\frac{1}{u}$ is the P wave velocity in surface (km/s), with an assumed average of 7 km/s in crustal

layer of Mendocino triple junction (*Henstock and Levander*, 2003). z is the crustal path between the station and the turning point. We applied a Moho depth correction using the crustal thickness beneath all stations from CRUST1.0 model *Laske et al.* (2013). p is the ray parameter of P_n wave given by $\frac{1}{u_m}$, the P wave velocity in the mantle, which we assumed a typical velocity of 8.2 km/s. Crustal thickness is the same for all stations in the CRUST1.0 model (Fig.A.1), hence, we applied the same Δ_{P_n} distance correction of 16.4 km and 2.7s in τ_{P_n} for all records to measure the travel times and epicentral distances. No crustal correction was applied for the epicenters because all focal depths (Table.1) are located below the crust in the uppermost mantle.

u_{P_n} uncertainties (δv) were calculated using a quantitative uncertainty equation of *Taylor* (1997) defined in function of the variables number,

$$\delta v = v\sqrt{\left(\frac{\delta\Delta}{\Delta}\right)^2 + \left(\frac{\delta\tau}{\tau}\right)^2} \tag{2.4}$$

in which $\delta\Delta$ and $\delta\tau$ refer to an assumed error of 5 km in epicentral distances and 1s in travel times. Our assumptions can be applied because the picking uncertainties existent in earthquake location processing of the global catalogs where it comes to the epicenter coordinates. Δ and τ are the final ray path distance and travel time after applying the Δ_{P_n} and τ_{P_n} corrections.

2.3 Temperatures in lithosphere

We modeled thermal structure beneath MFZ using methodology of *Sandwell and Schubert* (1982). The two-dimensional temperature variation (ΔT) across a fracture zone is

$$\Delta T(x,z,t) = T_s + \frac{1}{2}(T_m - T_s)\left[erfc\left(\frac{x}{2\sqrt{kt_{age_1}}}\right) erf\left(\frac{z}{2\sqrt{kt_{age_1}}}\right) + erfc\left(\frac{-x}{2\sqrt{kt_{age_1}}}\right) erf\left(\frac{z}{2\sqrt{kt_{age_2}}}\right)\right. \tag{2.5}$$

where z is the depth below the seafloor range applied in the model, k is the thermal diffusivity, and x the distance across the fracture zone. t_{age_1} and t_{age_2} are the lithospheric age of either side of the fracture zone. We assume $k = 8x10^{-7}m^2s^{-1}$ (*Parsons and Sclater*, 1977). T_m is an assumed mantle temperature of 1400°C. The model was applied in a horizontal length of 100 km to the north and 120 km south, referring to the area in which the OBEM instruments were deployed.

We calculated the mean temperature below the seafloor along each one of the ray paths, assuming a half-space cooling. We used the Moho depths of *Laske et al.* (2013) km-to-km along the ray path, and applied the lithospheric age variation to calculate the temperatures using

$$T(z,t) = (T_m - T_s)erf\left(\frac{z}{2\sqrt{kt_{age}}}\right) + T_s \tag{2.6}$$

in which T_s is a fixed temperature of 0°C in seafloor (*Sandwell and Schubert*, 1982) and (*Sandwell*, 1984). Two-dimensional and half-space model across MFZ is shown in Fig.2.5.

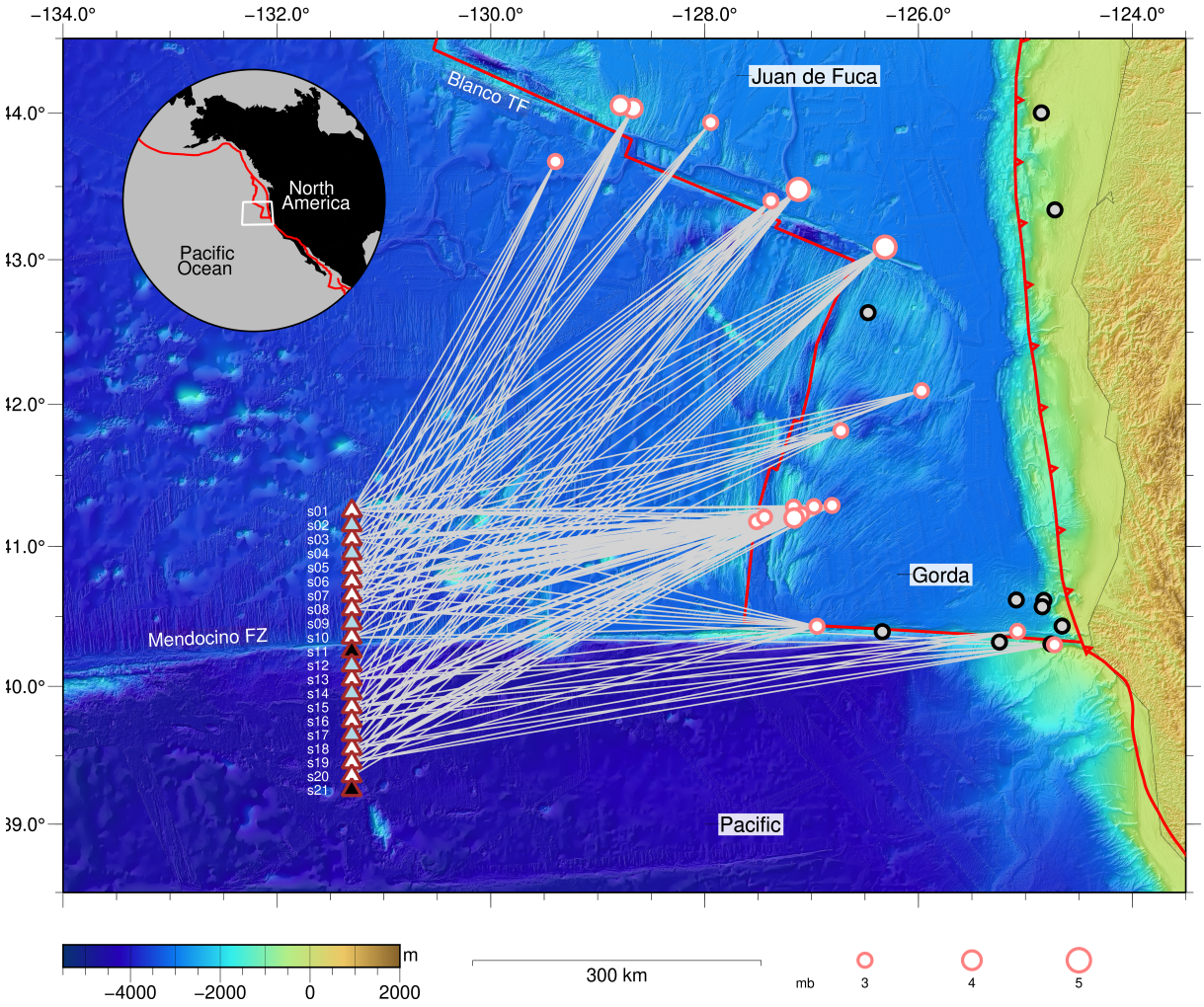

Figure 2.1. Bathymetric map over the study area in eastern Pacific ocean. Red-bordered triangles present the instruments deployed along the Mendocino Fracture Zone project (*Reyes-Ortega et al.*, 2019). Triangles with white/blue backgrounds are OBEM stations with data used/not used in research. Two stations of the network did not work along the deployment period (triangles with black background). White/gray circles are the events recorded/not recorded by the instruments.

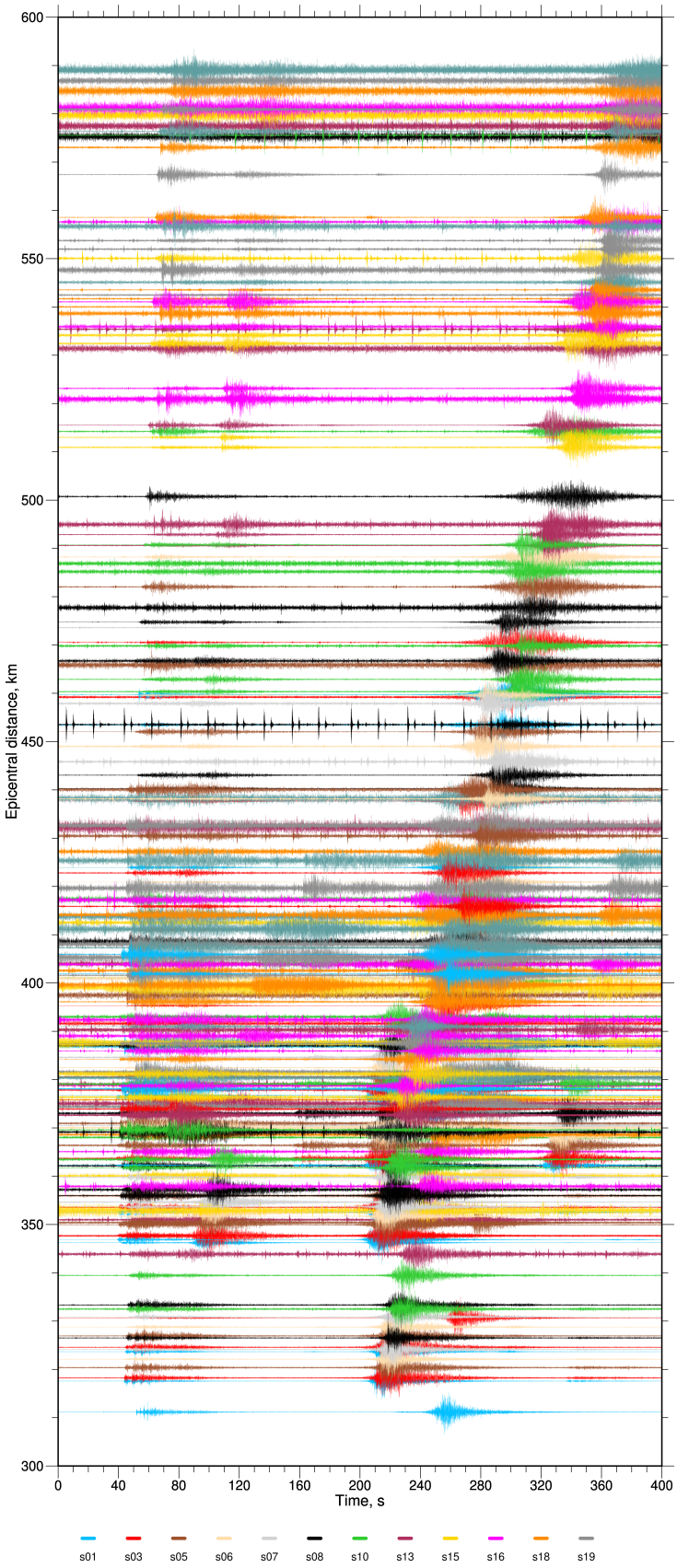

Figure 2.2. Waveforms of the 205 ray paths used in P_n velocities, with 2.5 Hz high-pass filter applied in the signal.

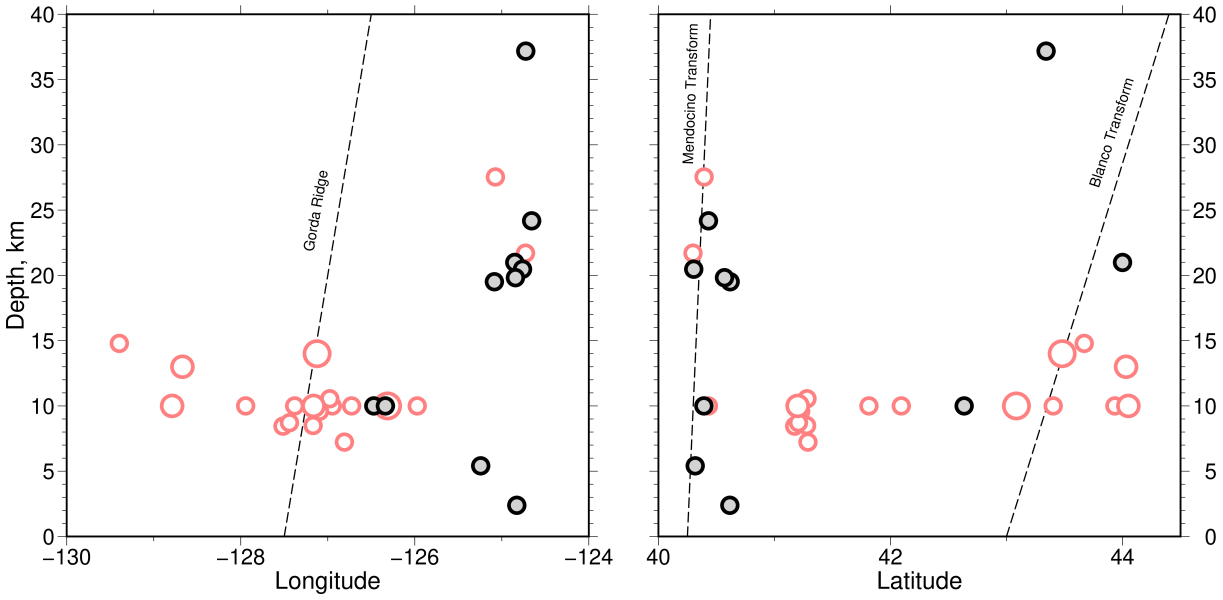

Figure 2.3. Longitude/latitude distribution of the epicenter used in this study from global catalogs, compared to the hypocenter depth (left/right graphic). Most earthquakes analyzed are shallower than 15 km.

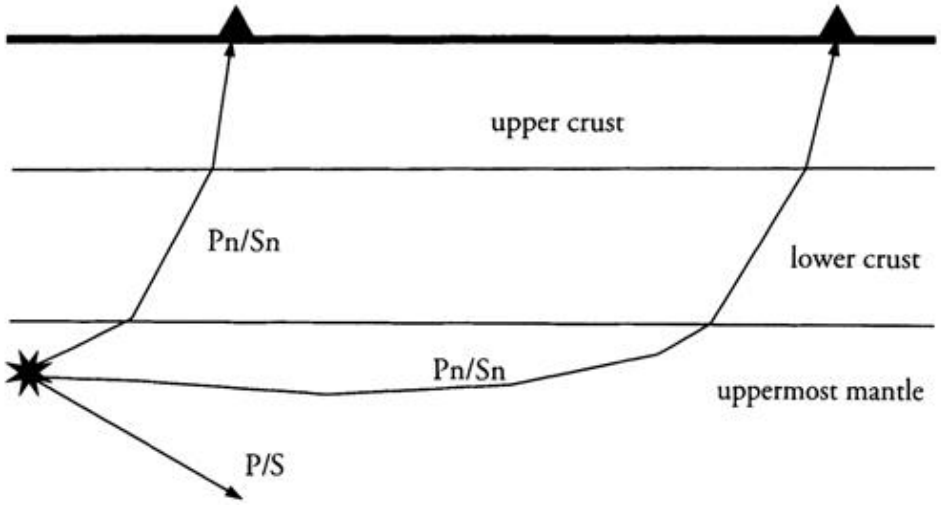

Figure 2.4. Illustration showing the layers in which travels the P_n and P phases shown by *Storchak et al.* (2003).

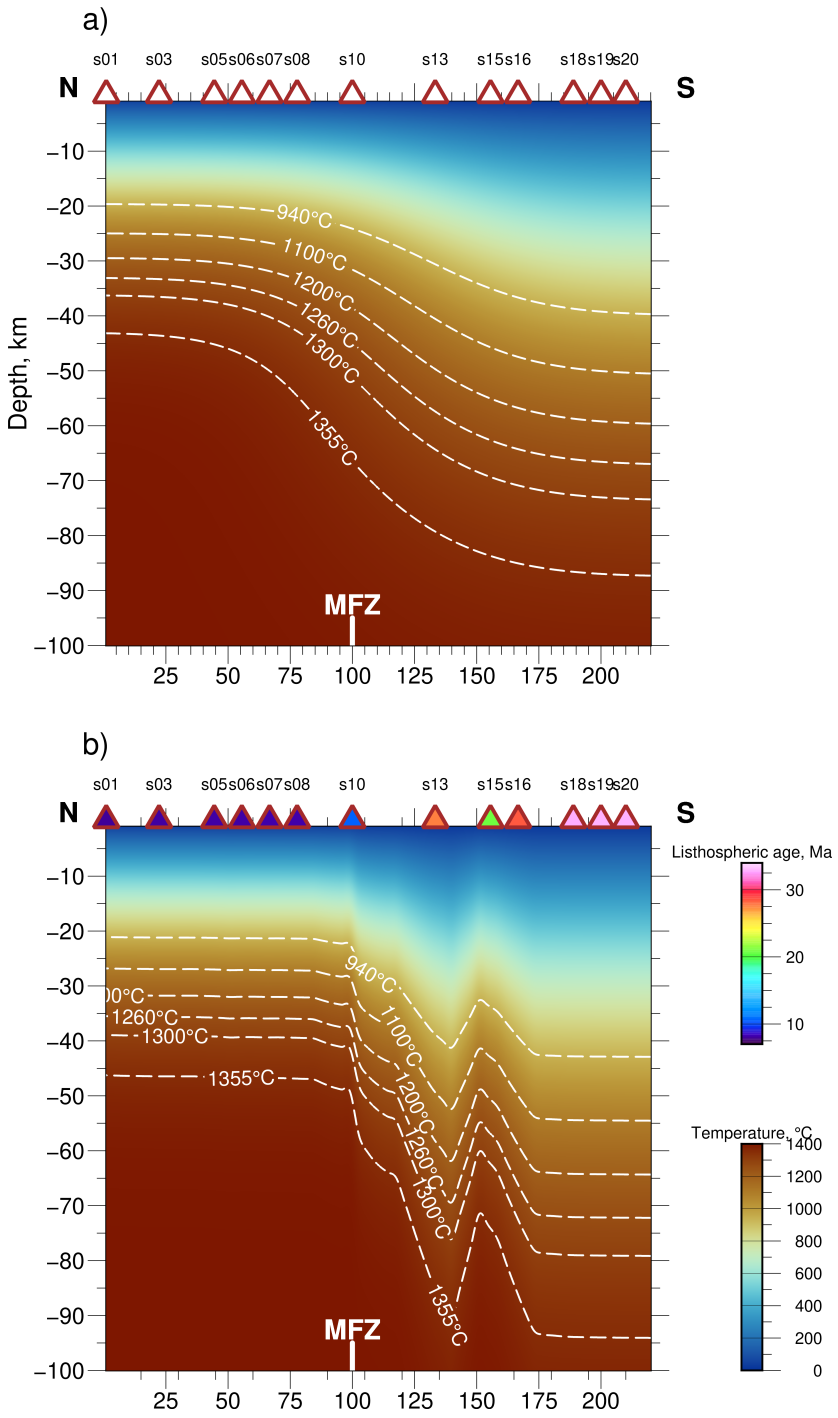

Figure 2.5. Thermal structure across Mendocino fracture zone along the 220 km extension of the OBEM instruments deployed area. a) Temperatures obtained from the two-dimensional model (eq.5) using the lithospheric ages of 8 and 33 Ma to the north and south sides of the fracture zone. The horizontal position of the fracture zone is presented by a white trace on the inferior horizontal axis. Triangles shown in the superior horizontal axis present the OBEM instruments across MFZ. Half-space thermal structure modeled using eq.1 is presented in b). Temperatures were calculated km by km using lithospheric ages of (*Müller et al.*, 2008). Triangle colors present the seafloor ages beneath the instruments.

Chapter 3

Measurements

3.1 Uppermost mantle velocities

A total of 205 P_n velocities were estimated using the one-directional ray paths of the 19 earthquakes recorded by the stations. Results showed P_n phases traveling from 8.01 to 8.48 km/s over the uppermost mantle beneath the study area (Fig.3.1), with uncertainties ranging $\pm$0.11-0.21 km/s. For these data, we found a predicted arrival time of the IASP91 model and observed P_n differing from 2.9 to 14.7 s (Fig.3.2a). This difference could be explained by factors such as uncertainty in CRUST1.0 thickness, epicenter location uncertainties, and the seafloor depth which varies along all instruments. Travel times demonstrate that most P_n velocities measured are faster than 8.2 km/s (Fig.3.2b).

P_n velocities do not show an uncertainty dependence on the travel-time increasing similar to (*de Melo et al.*, 2021). However, we observed variations in P_n velocities depending on both epicenter location and data source position (north or south side of the fracture zone). Three events with magnitude 3.0-3.2 and epicenter located over the active area of the Mendocino transform had velocities ranging between 8.24$\pm$0.13 and 8.48$\pm$0.19 km/s. In these cases, the azimuthal orientation of ray paths is roughly parallel to the transform fault. P_n phases of the three earthquakes traversed in lithosphere with age ranging from 13 to 33 Ma in the older side of the fracture zone (south). In contrast, the younger lithosphere has an age ranging from 0 to 8 Ma. The fastest P_n velocities correspond to propagating on the south side of the fracture zone (Fig.3.1).

Uppermost mantle velocities ranging from 8.04±0.18 until 8.40±0.15 km/s were estimated for seven earthquakes of magnitude 2.8-3.2 with epicenters located inside Gorda plate close to ∼41° latitude. P_n seismic tomography in the same area have similar velocities in 8.12-8.23 km/s range (*Buehler and Shearer*, 2017), as also hydrophone array with an average of 8.0±0.1 km/s *Slack et al.* (1999). Most ray paths are oriented obliquely to the spreading ridge and travel in lithosphere having ages 0-8 Ma to stations at the north side of MFZ. Ray paths to the stations on the south travel across both the spreading and fracture zone reaching the older lithosphere faster than the north side. Velocities obtained in the analysis of a 4.2 magnitude earthquake located close to the spreading ridge of Gorda plate are shown in Fig.3.3a. One single earthquake was located inside the Gorda plate (∼42°). Due to the weak magnitude at that distance, and the high attenuation on the western coast of the United States (*Buehler and Shearer*, 2014), it was only recorded on instruments in the younger side of MFZ, with P_n velocities from 8.0±0.13 to 8.1±0.14 km/s. Similarly, an earthquake located ∼41.8° latitude was only recorded by stations on the north side of MFZ and a single instrument on the south side. P_n ray velocities range from 8.02 to 8.26 km/s with uncertainties from 0.15 to 0.18 km/s. Seven epicenters are located in Blanco transform fault with magnitudes ranging from 3.0 to 5.4. Uppermost mantle P_n velocities range from 8.02-8.42 km/s with uncertainties from 0.11 to 0.22 km/s. The results are similar to P_n velocities of *Buehler and Shearer* (2017) which range from 8.05-8.15 km/s in the same area.

In contrast to the earthquakes located in Mendocino transform and Gorda plate, fast velocities were observed in the records of the ocean-bottom instruments deployed on the north side of the fracture zone. Examples of earthquakes showing the velocity variation on both sides of Mendocino are shown in Fig.3.3b. P_n ray paths were identified only in instruments on the north of Mendocino for two earthquakes with magnitudes 3.1 and 3.4. The two epicenters were not the farthest away, however, the hypocenter was deeper compared to the events in Blanco transform (Fig.2.3).

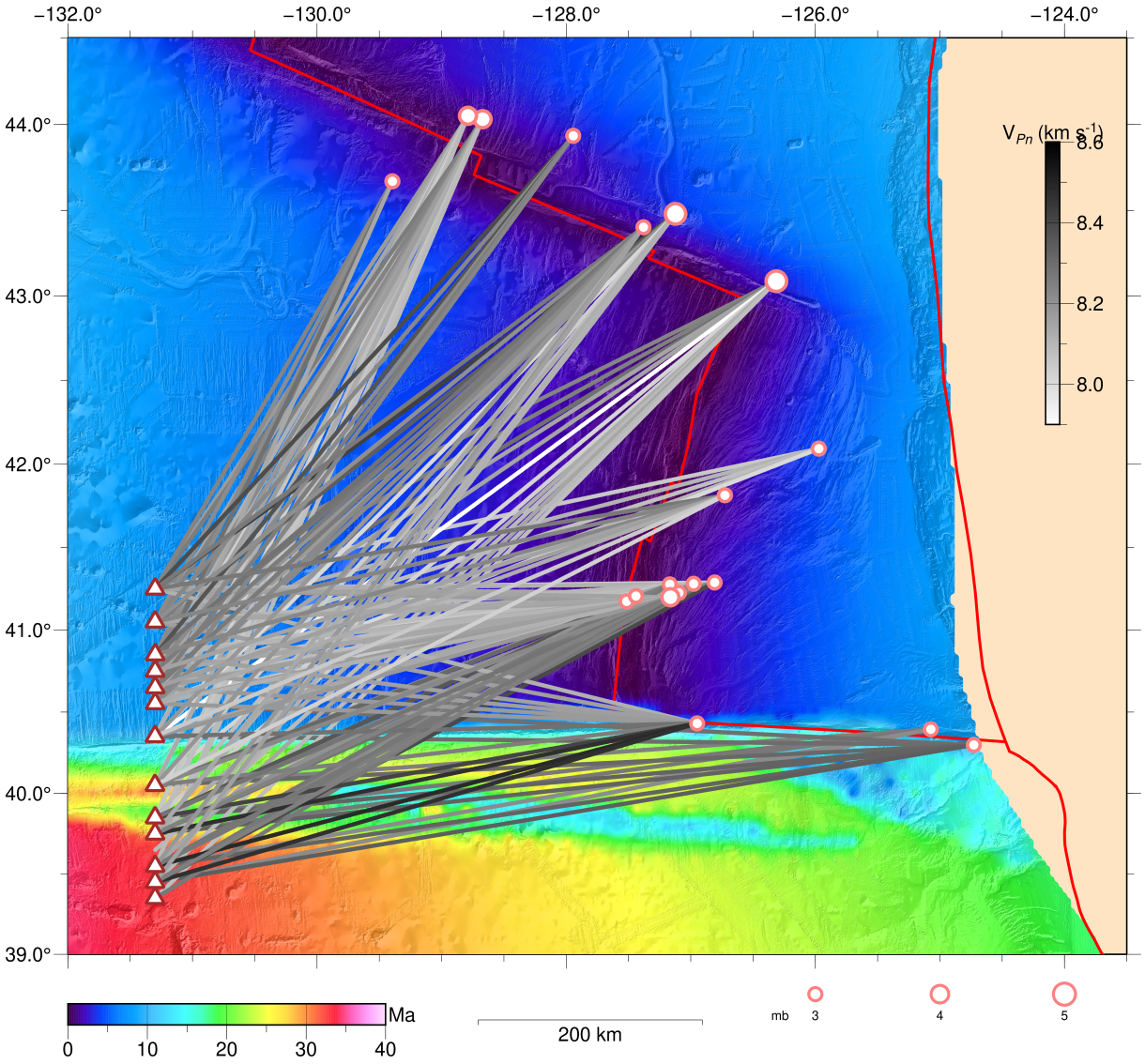

Figure 3.1. Lithospheric age map (*Müller et al.*, 2008) over Mendocino Fracture Zone area similar to the study area showing the stations used in the analysis, earthquakes, and ray paths (lines). White triangles are instruments with data used. The epicenter of the earthquakes used in P_n measurements is shown in colored white circles. Ray path lines are shaded by P_n velocities obtained in the analysis.

3.2 Moho temperature

We calculated the average temperature in the uppermost mantle-Moho along all ray paths using the half-space cooling formula of eq.2.6. The temperature was first calculated in a 1 km by 1 km grid using the lithospheric age model of *Müller et al.* (2008) together with the crustal thickness obtained from CRUST1.0 (*Laske et al.*, 2013). Fig.3.4 shows the thermal contrast along the coverage of all earthquakes.

In general, the highest temperatures occur along P_n ray paths crossing the Gorda ridge. Initial temperatures, ranging from 65-162°C, were observed along ray paths referring to three earthquakes located over the Mendocino Transform fault. The maximum temperature along the path nearest the transform fault reaches ∼459°C. Ray crosses the younger crust close to the Gorda ridge, in which the crustal thickness trend to be thinner compared to the surrounding (Fig.A.1). A different maximum temperature of ∼120°C occurs along ray paths traveling in older (10-33Ma) and thicker lithosphere on south side of MFZ, which has temperature averages ranging ∼65-92°C along ray pathway. Moho temperature at the epicenters located around Gorda ridge reach ∼1363°C when the ray crosses over the younger ridge (<2Ma). The average temperature varies from 120 to 230°C for record in stations on the younger side of MFZ, and 65-223°C in Moho over the thickest crust on the older side. These differences are recognized because the Moho temperature changes fast with the age in the oceanic lithosphere, in which thickness becomes influenced directly by changes in parameters such as the heat flow (*McKenzie et al.*, 2005). Ray paths associated with the single epicenter located inside of the Gorda plate cross Moho temperatures ranging from 220 to 234°C, with a maximum of ∼1293°C when the rays cross the spreading ridge and travel in direction to the instruments deployed in younger lithosphere in the north side of MFZ. In the Blanco transform fault, maximum temperatures vary from 427 to 680°C for earthquakes in middle of the transform valley where the ray paths are approximately transversal to the fault. Despite this, a higher temperature of 1365°C was obtained to the epicenter located in the east fracture zone where the ray paths already cross the

melting area in Gorda ridge (*Walowski et al.*, 2016). The average over the full ray paths of each earthquake in the Blanco transform ranges $\sim$149-235°C, with most rays situated over young lithosphere in north side of the fracture zone (Fig.3.4). These higher averages, when compared to MFZ, reflect the thinner Moho depth and younger lithosphere along the ray paths way of the Blanco transform.

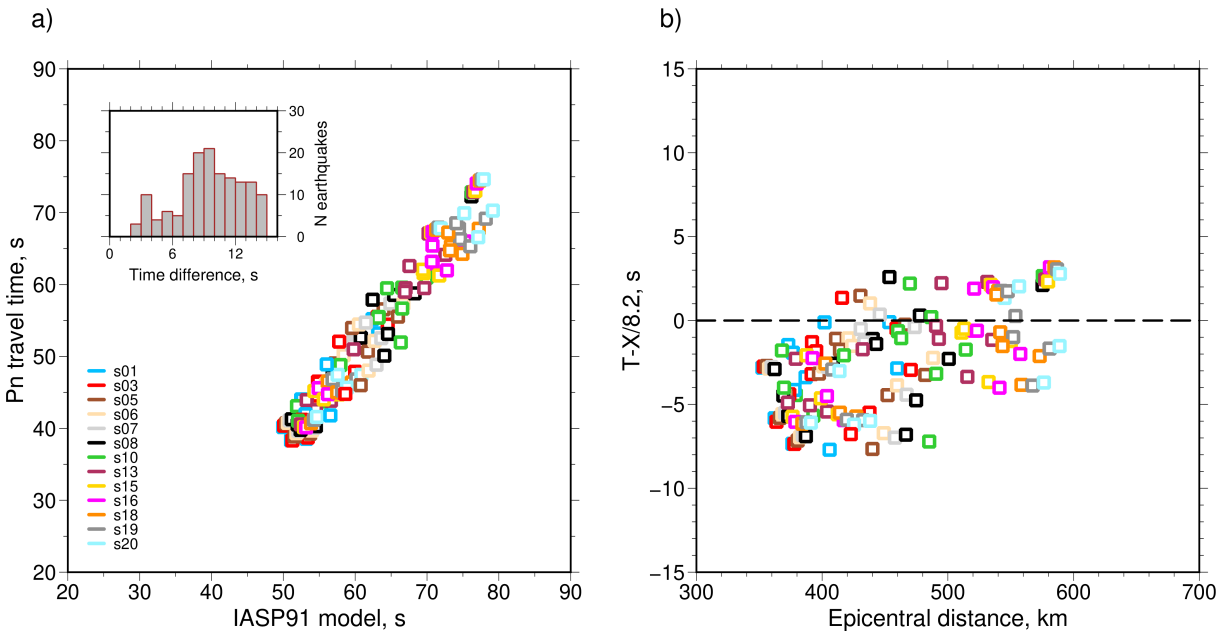

Figure 3.2. a) Squares represent the correlation between P_n travel times with the theoretical travel times referent to the IASP91 global model (*Kennett and Engdahl*, 1991). Square colors show the different instruments. b) Reduced travel time versus epicentral distance using a velocity of 8.2 km/s (solid line).

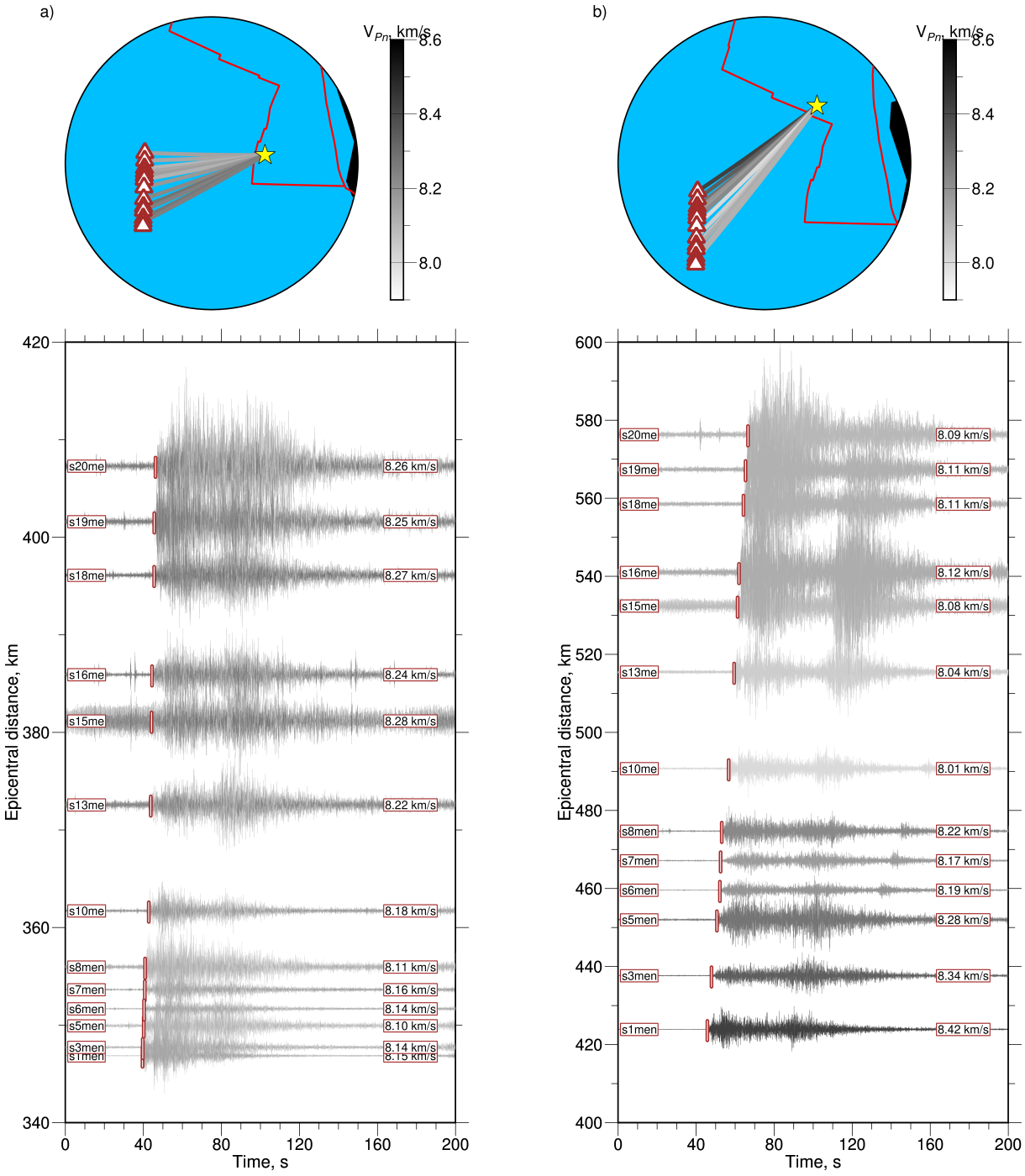

Figure 3.3. Waveform example of two earthquakes recorded by the 13 instruments (white squares plotted on the left side). a) mb 4.2 earthquake on October 18, 2017 located in Gorda ridge. b) A strike-slip earthquake with moment magnitude 5.4 on October 13, 2017, over Blanco transform fault. Waveform records are colored by P_n velocities (red squares on the right side of the signals). P_n arrival is presented by red vertical traces.

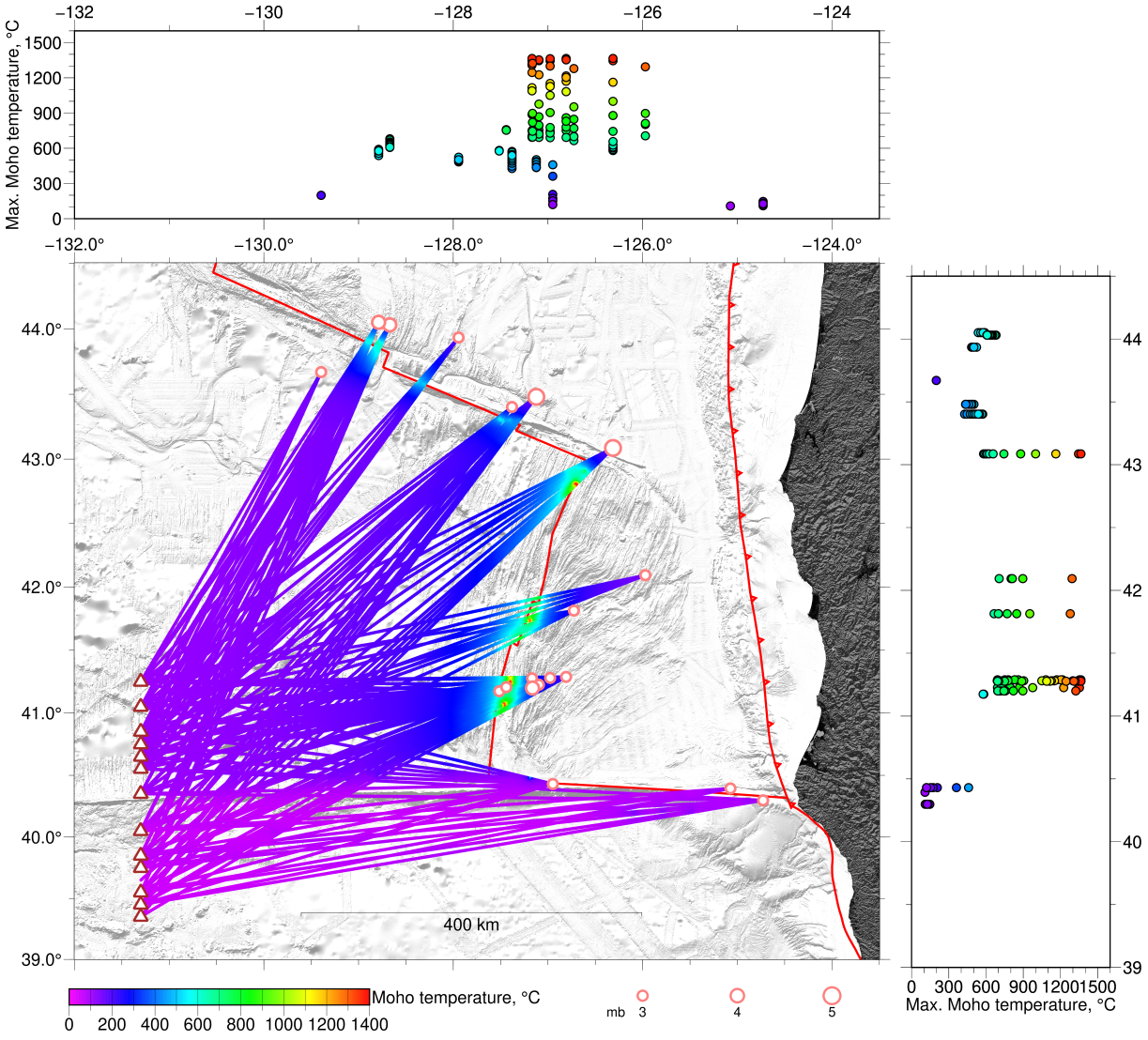

Figure 3.4. Map showing the temperatures at Moho depth based on seafloor age and crustal thickness. White triangle show the 13 OBEM instruments used, while epicenters are shown in white circles. P_n ray paths are shaded by the temperatures. Highest temperatures are observed along the ridge axis, compared to the rays inside the tectonic plate or over the transform faults. Shaded line colors in ray paths shows clearly the effect of the lithospheric age variation over the uppermost mantle temperate.

Chapter 4

Discussion

4.1 P_n velocities, age contrast, and seismic anisotropy

Previous studies have shown a correlation between compressional wave seismic velocities in layer 2A and crustal age in different ocean basins increasing rapidly until 50% in first 1Ma (*Grevemeyer and Weigel*, 1997), with velocities ranging from 2 to 5 km/s until 5 Ma (*Grevemeyer and Weigel* 1996; *Carlson* 1998). The effect of a rapid change in velocity over the younger crust arises as soon as moves out of the ridge axis where the upwelled mantle material is fastly cooling and solidifying. Other recent studies in equatorial Atlantic revealed that seismic velocities in 2A/2B layers increase rapidly both in young (e.g. *Vaddineni et al.* 2021) and in older lithosphere (e.g.*Audhkhasi and Singh* 2019) until 70 Ma with velocities reaching >6.5 km/s. Moreover, uppermost mantle P_n velocities have been measured with velocities ∼8 km/s across the St. Paul fracture zone with old lithospheric ages of ∼70 Ma on the north side and 40-50 Ma in the south (*Growe et al.*, 2021). Also, other analyses of the Mendocino fracture zone and East Pacific Rise show similar results with the P waves increasing their velocities parallel to the back-azimuth until approximately 90° (*Hess* 1964; *Backus* 1965; *Raitt et al.* 1969; *VanderBeek and Toomey* 2017). The effect can be recurrent to the uppermost mantle mineral alignment (e.g. olivine polycrystals) in which the rheologic directional support in strength changes the propagation velocity until 5% in surface waves (*Blackman et al.*, 2017) and 3.4% in P waves of Atlantic ocean (*Gaherty et al.*, 2004). *VanderBeek and Toomey* (2019) shown that P_n waves can varies until 1-8% in

Mendocino transform, Gorda ridge, and Blanco transform, due to the anisotropic viscous mantle 1 km beneath the Moho.

We compared the P_n velocities obtained to all source-receiver ray paths of Mendocino fracture zone with the lithospheric age average along ray paths using the global model of *Müller et al.* (2008), presented in Fig.4.1,a. We observed that there is a correlation between the increase of P_n seismic velocity parallel to the aging of the lithosphere independently of the epicentral distance (Fig.4.1a). Most ray paths are in lithosphere with ages $<$10 Ma and velocities range from 8.0-8.4 km/s. P_n velocities with a mean of 7.9 km/s and maximum reaching 8.9 km/s were identified by *de Melo et al.* (2021) in lithosphere of equatorial Atlantic having a similar age range ($<$10 Ma), however, with a colder and more complex uppermost mantle geodynamic (*Sichel et al.*, 2008). From 10 to 24 Ma lithospheric age in the P_n ray paths, the velocities slowly increase to $\sim$8.2 to $\sim$8.5 km/s in records of MFZ. We believe the P_n velocities beneath Mendocino fracture zone surrounding increase fast with aging like the effect on intern layers of the crust. However, the understanding will depend directly on the global lithospheric age model applied along the analysis and interpretation of the results.

Comparing the ray path orientation with the P_n seismic velocities (Fig.4.1,b,c) show the correlation between the P_n velocities and Back azimuth. We observed that most of these ray paths in older lithosphere were oriented to back-azimuth $>70^\circ$, with the highest velocities in $\sim 100^\circ$ (Fig.4.1b,c). P_n velocities $<70^\circ$ has in most velocities lower than 8.2 km/s and every them presenting average of lithospheric age $<$8 Ma. Despite the apparent lack of ray paths in some orientations, we believe there is a partial link of the seismic velocities variations with the anisotropic effect over the uppermost mantle material.

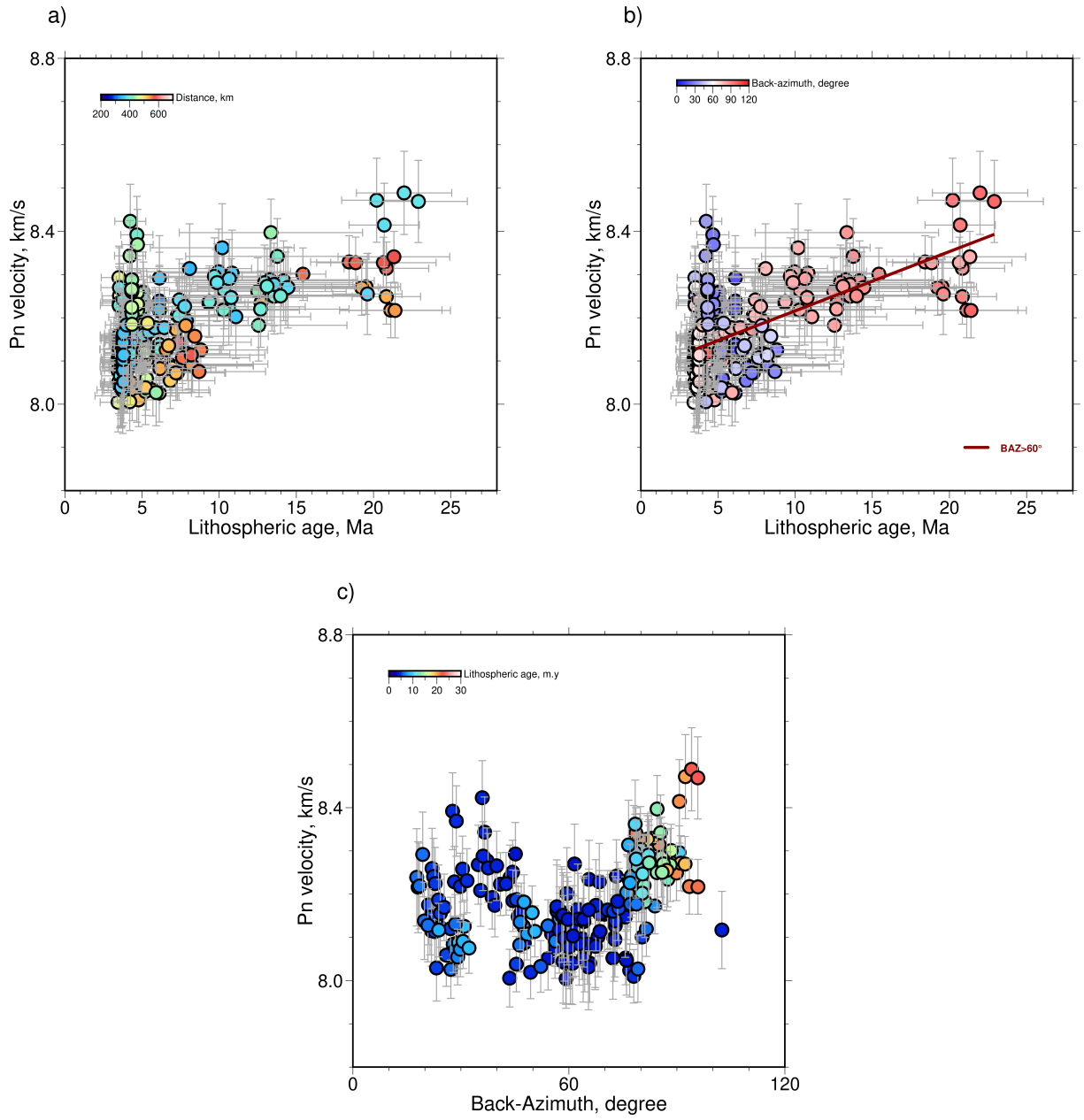

Figure 4.1. a) P_n velocities plotted against lithospheric age (*Müller et al.*, 2008). Circle colors represent the epicentral distance. Horizontal error bars are the standard deviation of lithospheric age along the ray paths. Vertical error bar the uncertainties of the uppermost mantle velocities. P_n velocity versus age are similarly shown in b). Differently, circle colors represent the back-azimuth angle of the ray path directions. Red line shows the trending for direction lines with back-azimuth above 60°, presenting an increase of velocity parallel to the back-azimuth. The same effect can be viewed in c) plot showing P_n velocity versus back-azimuth. Circles are colored by the mean lithospheric age.

4.2 P_n velocities and Moho temperature

Laboratory measurements show that seismic parameters such as the velocity and Q attenuation factor vary with temperature as well as differences in mineral and mantle composition (*Sobolev et al.* 1996; *Goes et al.*2000). These can explain the travel time anomalies of P_n wave observed in continental areas of the United States containing variation in mantle composition (*Herrin and Taggart* 1962; *Chung*1977). Other studies have observed agreement in the correlation between heat flow, mantle temperature, and P_n velocities (*Black and Braile* 1982; *Goes and van der Lee*2002; *Perry et al.*2006). However, most of these studies were from continent lithosphere. There are two studies of the P_n velocities in the oceanic uppermost mantle of Antarctica where authors note a possible link between variations of the P_n velocity, temperature, and heat flux (*An et al.* 2015; *Lucas et al.*2021). We have compared the P_n velocity average of each ray path with the uppermost mantle-Moho temperatures calculated in this study (Fig.3.4). P_n velocities show a systematic decrease with increasing Moho temperatures. A least squares regression has a slope dV_{P_n}/dT_{Moho} of -0.208 in MFZ (Fig.4.2). The correlation coefficient obtained in MFZ was different when compared to -0.44 identified by *Perry et al.* (2006) to peridotite rocks. However, there are some factors that should influence and limit our analysis. Firstly, the authors used Moho temperatures estimated from the heat flux, which is unlike the differences from the half-space cooling model. Secondly, we use Moho depths obtained from the global CRUST1.0 grid (*Laske et al.*, 2013), differently from *Perry et al.* (2006) where they used seismic refraction data. Last, the geodynamic conditions over the continental lithosphere in southern Canadian Shield (*Perry et al.*, 2006), in which the features differ totally from the oceanic lithosphere. In addition, *Faul and Jackson* (2005) observed a reduction in shear wave velocity with an increase of temperature over lithospheric ages of 2, 12, 35, 80, 112 Ma in Pacific ocean. Therefore, we can infer that the slowing of P_n velocities in Mendocino surroundings can depend directly on the average uppermost mantle-Moho temperatures along the source-receiver ray path.

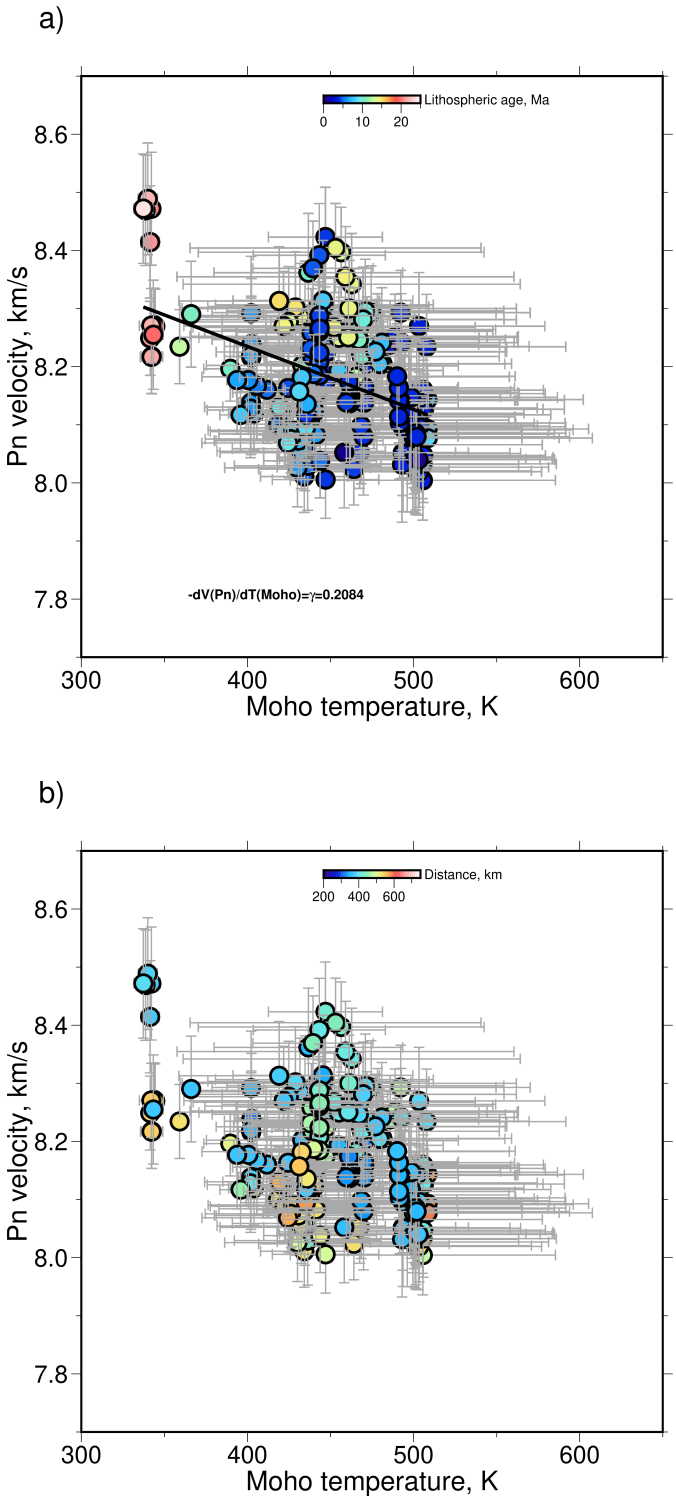

Figure 4.2. Correlation between uppermost mantle velocities and Moho temperature average. The standard deviation of the temperature variation along the ray path is shown in horizontal error bars. P_n velocity uncertainties are presented by vertical error bars. Circles are colored lithospheric age (*Müller et al.*, 2008) and distance in a/b figures.

Chapter 5

Conclusion

This study was realized using seismic waves recorded by a set of seafloor instruments deployed across the Mendocino fracture zone (MFZ) in 2017. We measured estimates of seismic uppermost mantle-Moho P_n velocity from the travel times of 205 ray paths over 13 instruments. We also used a thermal structure model across the deployment area to estimate the under-lithosphere boundaries.

We identified that the uppermost mantle-Moho seismic velocities across the Mendocino FZ and surrounding areas, having intermediate spreading rates increase as the lithosphere become older, with an average velocity of $\sim$8.1 km/s in younger ($<$10 Ma) and $\sim$8.4 in older (20 Ma) lithosphere, and sample thermal differences as well as anisotropy. Integrated ages are compared with average P_n velocities and show a systematic variation that agrees with models of P_n velocity versus temperature. P_n velocity anisotropy also partially agrees with previous studies. Therefore, our results corroborate that the uppermost mantle seismic velocities show a dependence on lithospheric age and Moho temperature in locations with mantle upwelling with intermediate rates over oceanic seafloor, despite the complex tectonic activity of areas such as Gorda plated where the seismic velocities scattering of is more variable in P_n ray paths originated in younger lithosphere over there.

This thesis, in full, is in preparation for publication as it may appear in a journal. de Melo, Guilherme W. S.; Sandwell, David T.; Constable, Steven. The thesis author was the primary

investigator and author.

Appendix A

Crustal thickness

We applied the CRUST1.0 global model of crustal thickness in measurements of the P_n velocity and Moho temperatures. The model was compiled by *Laske et al.* (2013) using elastic proprieties according to the basement or tectonic setting, using 1x1 degree cells along the oceanic lithosphere. The crustal thickness varies from ∼5.8 to ∼7.8 km along the study area (Fig.A.1).

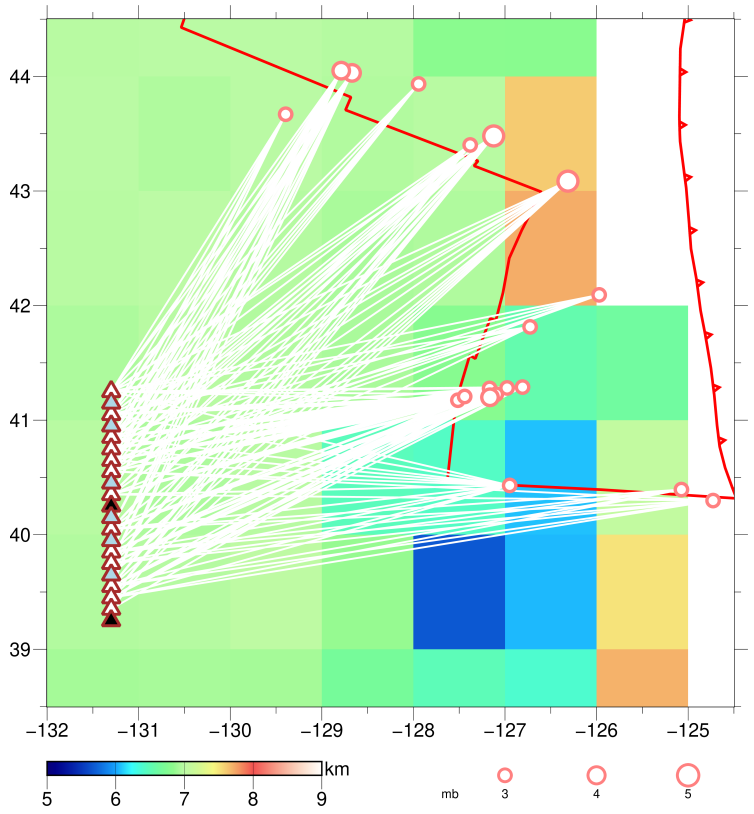

Figure A.1. Oceanic crustal thickness along study area obtained in CRUST1.0 global model.

Bibliography

An, M., D. A. Wiens, Y. Zhao, M. Feng, A. Nyblade, M. Kanao, Y. Li, A. Maggi, and J.-J. Lévêque (2015), Temperature, lithosphere-asthenosphere boundary, and heat flux beneath the antarctic plate inferred from seismic velocities, *Journal of Geophysical Research: Solid Earth*, *120*(12), 8720–8742.

Audhkhasi, P., and S. Singh (2019), Seismic structure of the upper crust from 0–75 ma in the equatorial atlantic ocean on the african plate using ultralong offset seismic data, *Geochemistry, Geophysics, Geosystems*, *20*(12), 6140–6162.

Backus, G. E. (1965), Possible forms of seismic anisotropy of the uppermost mantle under oceans, *Journal of Geophysical Research*, *70*(14), 3429–3439.

Black, P. R., and L. W. Braile (1982), Pn velocity and cooling of the continental lithosphere, *Journal of Geophysical Research: Solid Earth*, *87*(B13), 10,557–10,568.

Blackman, D., D. Boyce, O. Castelnau, P. Dawson, and G. Laske (2017), Effects of crystal preferred orientation on upper-mantle flow near plate boundaries: rheologic feedbacks and seismic anisotropy, *Geophysical Journal International*, *210*(3), 1481–1493.

Braunmiller, J., and J. Nábělek (2008), Segmentation of the blanco transform fault zone from earthquake analysis: Complex tectonics of an oceanic transform fault, *Journal of Geophysical Research: Solid Earth*, *113*(B7).

Buehler, J., and P. Shearer (2014), Anisotropy and vp/vs in the uppermost mantle beneath the western united states from joint analysis of pn and sn phases, *Journal of Geophysical Research: Solid Earth*, *119*(2), 1200–1219.

Buehler, J., and P. Shearer (2017), Uppermost mantle seismic velocity structure beneath usarray, *Journal of Geophysical Research: Solid Earth*, *122*(1), 436–448.

Buehler, J. S., and P. M. Shearer (2010), Pn tomography of the western united states using usarray, *Journal of Geophysical Research: Solid Earth*, *115*(B9).

Carlson, R. (1998), Seismic velocities in the uppermost oceanic crust: Age dependence and the

fate of layer 2a, *Journal of Geophysical Research: Solid Earth*, *103*(B4), 7069–7077.

Chung, D. (1977), Pn velocity and partial melting—discussion, *Tectonophysics*, *42*(1), T35–T42.

Cox, C., T. Deaton, and S. Webb (1984), A deep-sea differential pressure gauge, *Journal of Atmospheric and Oceanic Technology*, *1*(3), 237–246.

de Melo, G. W., R. Parnell-Turner, R. P. Dziak, D. K. Smith, M. Maia, A. F. do Nascimento, and J.-Y. Royer (2021), Uppermost mantle velocity beneath the mid-atlantic ridge and transform faults in the equatorial atlantic ocean, *Bulletin of the Seismological Society of America*, *111*(2), 1067–1079.

DeMets, C., R. G. Gordon, and D. F. Argus (2010), Geologically current plate motions, *Geophysical journal international*, *181*(1), 1–80.

Dengler, L., J. W. Dewey, R. McPherson, K. Moley, M. Murray, and M. Pasyanos (1995), *The September 1, 1994 Mendocino fault earthquake*.

Dziak, R., D. Bohnenstiehl, H. Matsumoto, C. Fox, D. Smith, M. Tolstoy, T. Lau, J. Haxel, and M. Fowler (2004), P-and t-wave detection thresholds, pn velocity estimate, and detection of lower mantle and core p-waves on ocean sound-channel hydrophones at the mid-atlantic ridge, *Bulletin of the Seismological Society of America*, *94*(2), 665–677.

Faul, U. H., and I. Jackson (2005), The seismological signature of temperature and grain size variations in the upper mantle, *Earth and Planetary Science Letters*, *234*(1-2), 119–134.

Gaherty, J. B., D. Lizarralde, J. A. Collins, G. Hirth, and S. Kim (2004), Mantle deformation during slow seafloor spreading constrained by observations of seismic anisotropy in the western atlantic, *Earth and Planetary Science Letters*, *228*(3-4), 255–265.

Glazner, A. F., and G. Schubert (1985), Flexure of the north american lithosphere above the subducted mendocino fracture zone and the formation of east-west faults in the transverse ranges, *Journal of Geophysical Research: Solid Earth*, *90*(B7), 5405–5409.

Goes, S., and S. van der Lee (2002), Thermal structure of the north american uppermost mantle inferred from seismic tomography, *Journal of Geophysical Research: Solid Earth*, *107*(B3), ETG–2.

Goes, S., R. Govers, Vacher, and P (2000), Shallow mantle temperatures under europe from p and s wave tomography, *Journal of Geophysical Research: Solid Earth*, *105*(B5), 11,153–11,169.

Goldstein, P., D. Dodge, M. Firpo, L. Minner, W. Lee, H. Kanamori, P. Jennings, and C. Kisslinger (2003), Sac2000: Signal processing and analysis tools for seismologists and engineers, *The IASPEI international handbook of earthquake and engineering seismology*, *81*, 1613–1620.

Grevemeyer, I., and W. Weigel (1996), Seismic velocities of the uppermost igneous crust versus age, *Geophysical Journal International*, *124*(2), 631–635.

Grevemeyer, I., and W. Weigel (1997), Increase of seismic velocities in upper oceanic crust: The "superfast" spreading east pacific rise at 14° 14's, *Geophysical Research Letters*, *24*(3), 217–220.

Growe, K., I. Grevemeyer, S. C. Singh, M. Marjanović, E. P. Gregory, C. Papenberg, V. Vaddineni, L. Gómez de La Peña, and Z. Wang (2021), Seismic structure of the st. paul fracture zone and late cretaceous to mid eocene oceanic crust in the equatorial atlantic ocean near 18° w, *Journal of Geophysical Research: Solid Earth*, *126*(11), e2021JB022,456.

Henstock, T. J., and A. Levander (2003), Structure and seismotectonics of the mendocino triple junction, california, *Journal of Geophysical Research: Solid Earth*, *108*(B5).

Herrin, E., and J. Taggart (1962), Regional variations in pn velocity and their effect on the location of epicenters, *Bulletin of the Seismological Society of America*, *52*(5), 1037–1046.

Hess, H. (1964), Seismic anisotropy of the uppermost mantle under oceans, *Nature*, *203*(4945), 629–631.

Kennett, B., and E. Engdahl (1991), Traveltimes for global earthquake location and phase identification, *Geophysical Journal International*, *105*(2), 429–465.

Laske, G., G. Masters, Z. Ma, and M. Pasyanos (2013), Update on crust1. 0—a 1-degree global model of earth's crust, in *Geophysical research abstracts*, vol. 15, p. 2658, EGU General Assembly Vienna, Austria.

Lonsdale, P. (2005), Creation of the cocos and nazca plates by fission of the farallon plate, *Tectonophysics*, *404*(3-4), 237–264.

Lucas, E. M., A. A. Nyblade, A. J. Lloyd, R. C. Aster, D. A. Wiens, J. P. O'Donnell, G. W. Stuart, T. J. Wilson, I. W. Dalziel, J. P. Winberry, and A. Huerta (2021), Seismicity and pn velocity structure of central west antarctica, *Geochemistry, Geophysics, Geosystems*, *22*(2), e2020GC009,471.

Marjanović, M., S. C. Singh, E. P. Gregory, I. Grevemeyer, K. Growe, Z. Wang, V. Vaddineni, M. Laurencin, H. Carton, L. Gómez de la Peña, and C. Filbrandt (2020), Seismic crustal structure and morphotectonic features associated with the chain fracture zone and their role in the evolution of the equatorial atlantic region, *Journal of Geophysical Research: Solid Earth*, *125*(10), e2020JB020,275.

McKenzie, D., J. Jackson, and K. Priestley (2005), Thermal structure of oceanic and continental lithosphere, *Earth and Planetary Science Letters*, *233*(3-4), 337–349.

Menard, H. W., and T. Atwater (1969), Origin of fracture zone topography, *Nature*, *222*(5198), 1037–1040.

Müller, R. D., M. Sdrolias, C. Gaina, and W. R. Roest (2008), Age, spreading rates, and spreading asymmetry of the world's ocean crust, *Geochemistry, Geophysics, Geosystems*, *9*(4).

Mutter, J. C., and J. A. Karson (1992), Structural processes at slow-spreading ridges, *Science*, *257*(5070), 627–634.

Parsons, B., and J. G. Sclater (1977), An analysis of the variation of ocean floor bathymetry and heat flow with age, *Journal of geophysical research*, *82*(5), 803–827.

Perry, H., C. Jaupart, J.-C. Mareschal, and N. Shapiro (2006), Upper mantle velocity-temperature conversion and composition determined from seismic refraction and heat flow, *Journal of Geophysical Research: Solid Earth*, *111*(B7).

Raitt, R., G. Shor Jr, T. Francis, and G. Morris (1969), Anisotropy of the pacific upper mantle, *Journal of Geophysical Research*, *74*(12), 3095–3109.

Reyes-Ortega, V., S. Constable, and S. Wang (2019), Investigation of the mendocino fracture zone with marine electromagnetic method, *2019*, IUGG19–3085.

Rollins, J. C., and R. S. Stein (2010), Coulomb stress interactions among m 5.9 earthquakes in the gorda deformation zone and on the mendocino fault zone, cascadia subduction zone, and northern san andreas fault, *Journal of Geophysical Research: Solid Earth*, *115*(B12).

Sandwell, D., and G. Schubert (1982), Lithospheric flexure at fracture zones, *Journal of Geophysical Research: Solid Earth*, *87*(B6), 4657–4667.

Sandwell, D. T. (1984), Thermomechanical evolution of oceanic fracture zones, *Journal of Geophysical Research: Solid Earth*, *89*(B13), 11,401–11,413.

Searle, R. (2013), *Mid-ocean ridges*, Cambridge University Press.

Shearer, P. M. (2019), *Introduction to seismology*, Cambridge university press.

Sichel, S. E., S. Esperança, A. Motoki, M. Maia, M. F. Horan, P. Szatmari, E. d. C. Alves, and S. L. Mello (2008), Geophysical and geochemical evidence for cold upper mantle beneath the equatorial atlantic ocean, *Revista Brasileira de Geofísica*, *26*, 69–86.

Slack, P. D., C. G. Fox, and R. P. Dziak (1999), P wave detection thresholds, pn velocity estimates, and t wave location uncertainty from oceanic hydrophones, *Journal of Geophysical Research: Solid Earth*, *104*(B6), 13,061–13,072.

Sobolev, S. V., H. Zeyen, G. Stoll, F. Werling, R. Altherr, and K. Fuchs (1996), Upper mantle temperatures from teleseismic tomography of french massif central including effects of composition, mineral reactions, anharmonicity, anelasticity and partial melt, *Earth and Planetary Science Letters*, *139*(1-2), 147–163.

Storchak, D. A., J. Schweitzer, and P. Bormann (2003), The iaspei standard seismic phase list, *Seismological Research Letters*, *74*(6), 761–772.

Taylor, J. (1997), *Introduction to error analysis, the study of uncertainties in physical measurements*.

Vaddineni, V. A., S. C. Singh, I. Grevemeyer, P. Audhkhasi, and C. Papenberg (2021), Evolution of the crustal and upper mantle seismic structure from 0–27 ma in the equatorial atlantic ocean at 2 43 s, *Journal of Geophysical Research: Solid Earth*, *126*(6), e2020JB021,390.

VanderBeek, B. P., and D. R. Toomey (2017), Shallow mantle anisotropy beneath the juan de fuca plate, *Geophysical Research Letters*, *44*(22), 11–382.

VanderBeek, B. P., and D. R. Toomey (2019), Pn tomography of the juan de fuca and gorda plates: implications for mantle deformation and hydration in the oceanic lithosphere, *Journal of Geophysical Research: Solid Earth*, *124*(8), 8565–8583.

Walowski, K. J., P. J. Wallace, M. A. Clynne, D. Rasmussen, and D. Weis (2016), Slab melting and magma formation beneath the southern cascade arc, *Earth and Planetary Science Letters*, *446*, 100–112.